J Ther Eng, Vol. 12, No. 2, pp. 684−701, March, 2026

Journal of Thermal Engineering
Web page info: https://jten.yildiz.edu.tr
DOI: 10.14744/thermal.0001110

Research Article

3D mathematical investigation of MHD flow imposed with bioconvective conditions over casson nanofluid induced by permeable surface utilizing lie symmetry transformation

Saloni GUPTA[1,*], Chinta Mani TIWARI[1]

[1]*Maharishi School of Science, Maharishi University of Information Technology, Lucknow, UP-226013, India*

ARTICLE INFO

Article history
Received: 31 January 2025
Revised: 04 May 2025
Accepted: 12 May 2025

Keywords:
3D MHD flow; Bioconvection; Buongiorno's Model; Casson Fluid; Chemical reaction; Lie symmetry analysis; Nanofluid; Shooting Method

ABSTRACT

In the current framework, consequence of three dimensional Magnetohydrodynamics bio-convective Casson nanofluid flow by permeable extending surface in the existence of gyrotactic micro-organisms and chemical reaction has been scrutinized. Lie group analysis has been performed along with Runge Kutta Fehlberg algorithm by utilizing shooting technique in MATLAB programming. This model has been solved to calculate the impact of Peclet number Pe ($0.1 \le Pe \le 10.0$), micro-organism concentration difference parameter κ ($0.1 \le \kappa \le 5.0$), Bio-convective Lewis number Lb ($0.1 \le Lb \le 0.9$), Gyrotactic microorganism Biot number Bi_3 ($1 \le Bi_3 \le 10$), thermal Biot number Bi_1 ($0.1 \le Bi_1 \le 2.0$, Concentration Biot number Bi_2 ($1 \le Bi_2 \le 5$), Permeability parameter K ($0.1 \le K \le 0.5$), Chemical reaction parameter C_r ($0 \le C_r \le 4$), Lewis number Le ($1 \le Le \le 20$), thermophoresis Nt ($0.5 \le Nt \le 2.5$), Brownian motion Nb ($0.1 \le Nb \le 5.0$), Prandtl number Pr ($0.732 \le Pr \le 20.0$), Magnetic parameter M ($1.5 \le M \le 3.5$) and Casson fluid parameter β ($0.1 \le \beta \le 0.9$). Flow features are exemplified quantitatively for above mentioned fluid parameters via graphs and tables. Additionally, graphs are plotted for physical quantities of interest for non-Newtonian nanofluid parameters. Motile density declines with augmentation in Bio-convective Lewis number Lb and Bio-convective constant κ. It is found that, with augmentation in thermal Biot number from 0.1-2.0, heat transfer rate falls down by 85.45% whereas mass transfer rate falls down by 51.95% for higher concentration Biot number from 1.0-5.0. Moreover, motile concentration de-escalates for higher Pe and κ. Ultimately, the results show that the output outcomes can be accurately predicted by the applied model.

Cite this article as: Gupta S, Tiwari CM. 3D mathematical investigation of MHD flow imposed with bioconvective conditions over casson nanofluid induced by permeable surface utilizing lie symmetry transformation. J Ther Eng 2026;12(2):684−701.

INTRODUCTION

Now days, researchers are working in the field of nanofluid because of its physical characteristics and uses in a variety of industries, particularly manufacturing, biomedicine, and industry. Research greatly benefits from the characteristics of nanofluids, especially their low resistivity

***Corresponding author.**
*E-mail address: saloni.20.jindal@gmail.com

This paper was recommended for publication in revised form by Editor-in-Chief Ahmet Selim Dalkılıç

and attractive thermophysical properties. Usman et al. [1] presented the Darcy theory to demonstrate the impact of MHD hybrid nanofluid flow over stretching sheet exponentially. Asghar et al. [2] showed the impact of slip conditions and joule heating over hybrid nanofluid induced by shrinking surface exponentially. Haque et al. [3] presented the magnetic field effect via heat transportation of nanofluid flow numerically. Numerical computation of ternary nanofluid flow induced by energy transportation over permeable sheet has been shown by Bilal et al. [4]. Algehyne et al. [5] discussed the energy transition over bioconvective nanofluid flow numerically. Takreem et al. [6] discussed the radiative ternary nanofluid flow via shape factor analysis. Rafique et al. [7] utilizing OHAM Williamson nanofluid model induced with thermal radiation and bioconvection by porous sheet. Afzal et al. [8] demonstrated the impact of 3D MHD nanofluid flow in presence of heat radiation. Atofarati et al. [9] presented a holistic analysis for heat transfer enhancement in nanofluids. Over permeable stretching surface, a numerical study has been done by Jubair et al. [10] to identify the impact of chemical reaction.

A vital area of research, fluid dynamics is essential to comprehending and improving a variety of natural and industrial systems. Complex fluids, like Casson fluids, have attracted a lot of attention among the many fluids that have been examined because of their special qualities and uses. Shear-thinning behaviour and a yield stress are characteristics of Casson fluids, a kind of non-Newtonian fluid. Research has recently focused on how Casson fluids behave when exposed to external stimuli like magnetic fields and porous heat sources, particularly when they are stretched. In order to optimize engineering applications, it is necessary to comprehend the complicated flow characteristics that can result from the interplay of various external elements with Casson fluids. Researchers have focused a great deal of emphasis on the thermo-physical features of non-Newtonian fluid applications in several scientific and engineering domains. These fluids are suitable for use in the pharmaceutical, chemical, and other industries. Nonetheless, there are some difficulties in studying non-Newtonian fluids. When stretched, Casson fluids, which are renowned for their capacity to record shear-thinning behaviour, display special properties. The first was Casson movement for printing ink type pigment oil suspensions [11]. Rao et al. [12] discussed the impact of thermal radiation in addition to chemical reaction induced by stretching surface in presence of 3D MHD nanofluid flow by applying similarity solutions. Ramamoorthy and Pallavarapu [13] presented the impact of Williamson fluid flow induced by heat radiation. Influence of Viscous and Ohmic dissipation influenced by MHD Casson nanofluid flow has been presented by Vinita et al. [14] by following Runge Kutta Fehlberg algorithm. Ahmed M. Megahed [15] found the impact of heat radiation in presence of Williamson fluid. Reeshan et al. [16] discussed the optimization of hybrid nanofluid flow induced by MHD Casson fluid flow utilizing computational intelligence approach. Numerical modeling of motile microbes induced by porous medium in presence of activation energy was presented by Waseem et al. [17]. Swain et al. [18] discussed the presence of viscous dissipation effect utilizing Homotopy perturbation method induced by stretching surface. Influence of ternary hybrid nanofluid over stretching sheet in presence of MHD flow has been presented by Swain et al. [19]. Sahoo et al. [20] showed the impact of entropy generation induced by inclined plate in presence of MHD hybrid nanofluid flow.

The interaction of conducting fluids with an electromagnetic field is known as magnetohydrodynamics. Since some sheet materials lack a heat exchanger, rheostat flow kinematics is a practical application of magnetohydrodynamic in which a magnetic field is employed in traditional fluids. Additional applications include power storage, thermal insulation, and more. Given this, the magnetohydrodynamic (MHD) flow across a stretching sheet offers a wide range of industrial and manufacturing uses, such as continuous metal casting, polymer extrusion, the petroleum industry, and electrical power generators. The magnetohydrodynamic (MHD) effects that arise when Casson fluids are exposed to magnetic fields add complexity to the flow behaviour and have a major impact on fluid dynamics and heat transfer. Varatharaj et al. [21] presented the impact of heat radiation and transport phenomenon over hybrid nanofluid in presence of MHD flow. Adeyemi et al. [22] discussed the influence of thermal radiation and generation over MHD fluid flow. Akinbo et al. [23] implemented the impact of chemical reaction and heat radiation utilizing Walters' B fluid in presence of stagnation point flow. Elhag et al. [24] demonstrated the influence of bio-convective gyrotactic microorganism induced by 3D sheet. Dang et al. [25] discussed the impact of chemical reaction over MHD nanofluid flow in presence of convective conditions by utilizing RKF technique following shooting algorithm. Sowmiya et al. [26] analysed the impact of heat flux over Casson fluid flow in presence of MHD convective conditions. Irshad et al. [27] presented the numerical study of Casson fluid flow in porous medium induced by stretching surface. Mehmood et al. [28] discussed the conical gap between cone and rotating discover blood flow in presence of Casson nanofluid computationally. Azar et al. [29] analyze the impact of Casson fluid flow in presence of MHD flow over porous medium.

One useful method for examining nonlinear partial differential equations is Lie group analysis. Lie and Ackerman's work [30] shows how this method was developed, while [31] unifies known exact integration techniques that take differential equations into account. The Lie group analysis method was used by numerous researchers to examine a variety of fluid flow problems under various conditions [32–35]. Disu and Salawu [36] presented the impact of temperature distribution influenced by fluid flow over porous medium in presence of magnetohydrodynamic flow by applying Lie symmetry analysis. Nabwey et al. [37]

discussed influence of convecting heating and Navier slip ferrofluid flow in presence of radiation effect by using Lie group analysis. Influence of tangent hyperbolic fluid flow induced by shrinking sheet has been presented by Swain et al. [38]. Impact of 3D MHD nanofluid flow induced by thermal laminated sheet has been presented by Akbar et al. [39]. Tufail et al. [40] using Lie group approach to analyze the impact of slip conditions over Maxwell fluid induced by shrinking sheet. Over straining surface, Shahbaz Ali [41] discussed the influence of slip conditions in presence of Bingham plastic flow utilizing Lie group analysis.

Our problem's primary goal is to determine the transportation behaviour of MHD nanofluids using Lie group similarity solution and RKF technique by following shooting algorithm over 3D permeable stretching surface. Metallurgical processes in the industrial sector include continuous filament drawing via static fluids, copper wire annealing and tinning, the production of plastic and rubber sheets, crystal development, continuous cooling, and fibre spinning, among many more uses. Along with the chemical reaction and gyrotactic microorganisms, the surface in this problem is permeable stretching surface, causing the viscosity to change with temperature and concentration over 3D sheet. On this system, we have additionally applied a magnetic field. Here, the viscosity exhibits a linear relationship with temperature, and the Lie group similarity technique yielded self-similar differential equations. The Lie group of transformations is used to identify all of the problem's symmetries and then determine which of them can be employed to produce group-invariant, or more precisely, similarity solutions.

MATHEMATICAL MODEL

A constant bio-nanofluid stagnation point flow in three dimensions with Casson fluid flow in presence of chemical reaction, variable transport characteristics, and thermal convective boundary conditions is taken into consideration. A two component Buongiorno's model has been followed in presence of Brownian motion and thermophoresis parameter. Because of the phenomena known as bio-convection, the imposition of microorganisms into the nanofluid is only necessary to stabilize the tiny nanoparticles. Furthermore, it is thought that the nanoparticles have no effect on the microorganisms' ability to swim or their velocity. Additionally, it is a reasonable assumption that nanoparticle dilution (suspension) is prepared with very small amounts (i.e., 1%) in order to avoid the instability of bio-convection; otherwise, the higher concentration distribution of nanoparticles leads to the highly effective saturation (suspension) viscosity, which ultimately suppresses the given bio-convective flow. Figure 1 displays the physical model of the problem along with sheet's velocities u and v in the x and y directions, respectively. These presumptions and the conventional boundary layer approximation result in the following governing equations.

$$\frac{\partial \bar{u}}{\partial \bar{x}} + \frac{\partial \bar{v}}{\partial \bar{y}} + \frac{\partial \bar{w}}{\partial \bar{z}} = 0. \tag{1}$$

$$\bar{u}\left(\frac{\partial \bar{u}}{\partial \bar{x}}\right) + \bar{v}\left(\frac{\partial \bar{u}}{\partial \bar{y}}\right) + \bar{w}\left(\frac{\partial \bar{u}}{\partial \bar{z}}\right) = \nu\left(1+\frac{1}{\beta}\right)\left(\frac{\partial^2 \bar{u}}{\partial \bar{z}^2}\right) - \left[\left(\frac{\sigma {B_0}^2}{\rho}\right) + \left(\frac{\nu}{k_1}\right)\left(1+\frac{1}{\beta}\right)\right]\bar{u} \tag{2}$$

$$\bar{u}\left(\frac{\partial \bar{v}}{\partial \bar{x}}\right) + \bar{v}\left(\frac{\partial \bar{v}}{\partial \bar{y}}\right) + \bar{w}\left(\frac{\partial \bar{v}}{\partial \bar{z}}\right) = \nu\left(1+\frac{1}{\beta}\right)\left(\frac{\partial^2 \bar{v}}{\partial \bar{z}^2}\right) - \left[\left(\frac{\sigma {B_0}^2}{\rho}\right) + \left(\frac{\nu}{k_1}\right)\left(1+\frac{1}{\beta}\right)\right]\bar{v} \tag{3}$$

$$\bar{u}\left(\frac{\partial T}{\partial \bar{x}}\right) + \bar{v}\left(\frac{\partial T}{\partial \bar{y}}\right) + \bar{w}\left(\frac{\partial T}{\partial \bar{z}}\right) = \left(\frac{k}{(\rho C_p)_f}\right)\left(\frac{\partial^2 T}{\partial \bar{z}^2}\right) + \left(\frac{(\rho C_p)_p}{(\rho C_p)_f}\right) \times \left[D_B\left(\frac{\partial C}{\partial \bar{z}}\right)\left(\frac{\partial T}{\partial \bar{z}}\right) + \left(\frac{D_T}{T_\infty}\right)\left(\frac{\partial T}{\partial \bar{z}}\right)^2\right] \tag{4}$$

$$\bar{u}\left(\frac{\partial C}{\partial \bar{x}}\right) + \bar{v}\left(\frac{\partial C}{\partial \bar{y}}\right) + \bar{w}\left(\frac{\partial C}{\partial \bar{z}}\right) = D_B\left(\frac{\partial^2 C}{\partial \bar{z}^2}\right) + \left(\frac{D_T}{T_\infty}\right)\left(\frac{\partial^2 T}{\partial \bar{z}^2}\right) - K_r(C - C_\infty) \tag{5}$$

$$\bar{u}\left(\frac{\partial N}{\partial \bar{x}}\right) + \bar{v}\left(\frac{\partial N}{\partial \bar{y}}\right) + \bar{w}\left(\frac{\partial N}{\partial \bar{z}}\right) + \left(\frac{bW_c}{C_w - C_\infty}\right)\left[\frac{\partial}{\partial \bar{z}}\left(N\left(\frac{\partial C}{\partial \bar{z}}\right)\right)\right] = D_N\left(\frac{\partial^2 N}{\partial \bar{z}^2}\right) - K_r(N - N_\infty) \tag{6}$$

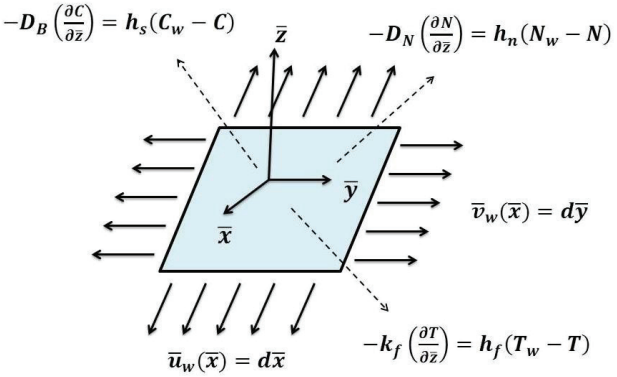

Figure 1. Physical Diagram.

To find similarity transformation for the current problem, the following dimensionless variables are introduced

$$x = \frac{\bar{x}}{\sqrt{\frac{\nu}{d}}},\ y = \frac{\bar{y}}{\sqrt{\frac{\nu}{d}}},\ z = \frac{\bar{z}}{\sqrt{\frac{\nu}{d}}},\ u = \frac{\bar{u}}{\sqrt{\nu d}},\ v = \frac{\bar{v}}{\sqrt{\nu d}},$$
$$w = \frac{\bar{w}}{\sqrt{\nu d}},\ \Theta = (T - T_\infty)/(T_w - T_\infty),$$
$$\Phi = (C - C_\infty)/(C_w - C_\infty),\ \chi = (N - N_\infty)/(N_w - N_\infty) \tag{7}$$

The boundary conditions are defined following as

$$\bar{u} = \bar{u}_w = d\bar{x}, \bar{v} = \bar{v}_w = d\bar{y}, \bar{w} = 0,$$
$$-k_f\left(\frac{\partial T}{\partial \bar{z}}\right) = h_f(T_w - T), -D_B\left(\frac{\partial C}{\partial \bar{z}}\right) = h_s(C_w - C),$$
$$-D_N\left(\frac{\partial N}{\partial \bar{z}}\right) = h_n(N_w - N)\ at\ \bar{z} = 0, \quad (8)$$
$$\bar{u} \to 0, \bar{v} \to 0, T \to T_\infty, C \to C_\infty, N \to N_\infty\ as\ \bar{z} \to \infty$$

Eq's. (1)-(6) takes the form

$$\frac{\partial u}{\partial x} + \frac{\partial v}{\partial y} + \frac{\partial w}{\partial z} = 0 \quad (9)$$

$$u\frac{\partial u}{\partial x} + v\frac{\partial u}{\partial y} + w\frac{\partial u}{\partial z} = \nu\left(1 + \frac{1}{\beta}\right)\frac{\partial^2 u}{\partial z^2} - \left[\frac{\sigma {B_0}^2}{d\rho} + \left(\frac{\nu}{dk_1}\right)\left(1 + \frac{1}{\beta}\right)\right] u \quad (10)$$

$$u\frac{\partial v}{\partial x} + v\frac{\partial v}{\partial y} + w\frac{\partial v}{\partial z} = \nu\left(1 + \frac{1}{\beta}\right)\frac{\partial^2 v}{\partial z^2} - \left[\frac{\sigma {B_0}^2}{d\rho} + \left(\frac{\nu}{dk_1}\right)\left(1 + \frac{1}{\beta}\right)\right] v \quad (11)$$

$$u\frac{\partial \Theta}{\partial x} + v\frac{\partial \Theta}{\partial y} + w\frac{\partial \Theta}{\partial z} = \left(\frac{k}{\nu(\rho C_p)_f}\right)\frac{\partial^2 \Theta}{\partial z^2} + \left(\frac{(\rho C_p)_p}{(\rho C_p)_f}\right) \times\left[\left(D_B\frac{C_\infty - C_\infty}{\nu}\right)\left(\frac{\partial \Phi}{\partial z}\right)\left(\frac{\partial \Theta}{\partial z}\right) + \frac{D_T(T_w - T_\infty)}{\nu T_\infty}\left(\frac{\partial \Theta}{\partial z}\right)^2\right] \quad (12)$$

$$u\frac{\partial \Phi}{\partial x} + v\frac{\partial \Phi}{\partial y} + w\frac{\partial \Phi}{\partial z} = \left(\frac{D_B}{\nu}\right)\frac{\partial^2 \Phi}{\partial z^2} + \left[\frac{D_T(T_w - T_\infty)}{\nu T_\infty(C_w - C_\infty)}\right]\partial^2\Theta/\partial z^2 - \left(\frac{K_r}{d}\right)\Phi \quad (13)$$

$$u\frac{\partial \chi}{\partial x} + v\frac{\partial \chi}{\partial y} + w\frac{\partial \chi}{\partial z} + \left(\frac{bW_c}{\nu}\right)\left[\left(\frac{N_\infty}{N_w - N_\infty}\right)\frac{\partial^2 \chi}{\partial z^2} + \chi\frac{\partial^2 \Phi}{\partial z^2} + \left(\frac{\partial \chi}{\partial z}\right)\left(\frac{\partial \Phi}{\partial z}\right)\right] = \left(\frac{D_N}{\nu}\right)\frac{\partial^2 \chi}{\partial z^2} - \left(\frac{K_r}{d}\right)\chi \quad (14)$$

along with the boundary conditions:

$$u = x, v = y\ at\ w = 0$$
$$\frac{\partial \Theta}{\partial z} = -B_{i1}(1 - \Theta), \frac{\partial \Phi}{\partial z} = -B_{i2}(1 - \Phi),$$
$$\frac{\partial \chi}{\partial z} = -B_{i3}(1 - \chi)\ at\ z = 0 \quad (15)$$
$$u \to 0,\ v \to 0, \Theta \to 0, \Phi \to 0, \chi \to 0\ as\ z \to \infty$$

LIE GROUP ANALYSIS

PDEs are difficult and computationally costly to solve numerically. The objective is to convert the PDEs in Equations (10)–(16) into ODEs. We accomplish this by converting PDEs to ODEs using the group approach. We apply the scaling group transformation in this work. Since it is difficult to solve the system of partial differentiation equations (7)–(9) with the B.C's (10) we use lie group transformations to convert the system into matching ordinary differential equations. Thus

$$x = e^{-\varepsilon c_1}x^*, y = e^{-\varepsilon c_2}y^*, z = e^{-\varepsilon c_3}z^*, u = e^{-\varepsilon c_4}u^*,$$
$$v = e^{-\varepsilon c_5}v^*, w = e^{-\varepsilon c_6}w^*, \Theta = e^{-\varepsilon c_7}\Theta^*, \Phi = e^{-\varepsilon c_8}\Phi^*, \quad (16)$$
$$\chi = e^{-\varepsilon c_9}\chi^*$$

Here, c_i; $1 \le i \le 9$ are arbitrary real integers that are not all zero at once, and ε is the group scaling parameter. When we enter eq. (11) into eq's. (7)-(10), we get

$$\frac{\partial u^*}{\partial x^*}\cdot e^{\varepsilon(c_1 - c_4)} + \frac{\partial v^*}{\partial y^*}\cdot e^{\varepsilon(c_2 - c_5)} + \frac{\partial w^*}{\partial z^*}\cdot e^{\varepsilon(c_3 - c_6)} = 0 \quad (17)$$

$$\frac{u^*\partial u^*}{\partial x^*}\cdot e^{\varepsilon(c_1 - 2c_4)} + \frac{v^*\partial u^*}{\partial y^*}\cdot e^{\varepsilon(c_2 - c_4 - c_5)} + w^*\frac{\partial u^*}{\partial z^*}\cdot e^{\varepsilon(c_3 - c_4 - c_6)} = \nu\left(1 + \frac{1}{\beta}\right)\frac{\partial^2 u^*}{\partial {z^*}^2}e^{\varepsilon(2c_3 - c_4)} - [\sigma {B_0}^2/d\rho + (\nu/dk_1)(1 + 1/\beta)]e^{-\varepsilon c_4}u^* \quad (18)$$

$$\frac{u^*\partial v^*}{\partial x^*}\cdot e^{\varepsilon(c_1 - c_4 - c_5)} + \frac{v^*\partial v^*}{\partial y^*}\cdot e^{\varepsilon(c_2 - 2c_5)} + w^*\frac{\partial v^*}{\partial z^*}\cdot e^{\varepsilon(c_3 - c_5 - c_6)} = \nu\left(1 + \frac{1}{\beta}\right)\partial^2 v^*/\partial {z^*}^2\, e^{\varepsilon(2c_3 - c_5)} - [\sigma {B_0}^2/d\rho + (\nu/dk_1)(1 + 1/\beta)]e^{-\varepsilon c_5}v^* \quad (19)$$

$$u^*\left(\frac{\partial \Theta^*}{\partial x^*}\right)e^{\varepsilon(c_1 - c_4 - c_7)} + \frac{v^*\partial \Theta^*}{\partial y^*}\cdot e^{\varepsilon(c_2 - c_5 - c_7)} + w^*\frac{\partial \Theta^*}{\partial z^*}\cdot e^{\varepsilon(c_3 - c_6 - c_7)} = [k / (\nu(\rho C_p)_f)]\,(\partial^2\Theta^*/\partial {z^*}^2)\, e^{\varepsilon(2c_3 - c_7)} + [(\rho C_p)_p / (\rho C_p)_f][\left(D_B\frac{(C_w - C_\infty)}{\nu}\right)\left(\frac{\partial \Phi^*}{\partial z^*}\right)\left(\frac{\partial \Theta^*}{\partial z^*}\right) e^{\varepsilon(2c_3 - c_7 - c_8)} + \left(D_T\frac{(T_w - T_\infty)}{(\nu T_\infty)}\right)\left(\frac{\partial \Theta^*}{\partial z^*}\right)^2 e^{\varepsilon(2c_3 - c_7)}] \quad (20)$$

$$u^*\left(\frac{\partial \Phi^*}{\partial x^*}\right)e^{\varepsilon(c_1 - c_4 - c_8)} + \frac{v^*\partial \Phi^*}{\partial y^*}e^{\varepsilon(c_2 - c_5 - c_8)} + w^*\frac{\partial \Phi^*}{\partial z^*}e^{\varepsilon(c_3 - c_6 - c_8)} = \left(\frac{D_B}{\nu}\right)\left(\frac{\partial^2 \Phi}{\partial {z^*}^2}\right)e^{\varepsilon(2c_3 - c_8)} + \left(\frac{D_T(T_w - T_\infty)}{\nu T_\infty(C_w - C_\infty)}\right)\left(\frac{\partial^2 \Theta}{\partial {z^*}^2}\right)e^{\varepsilon(2c_3 - c_7)} - \left(\frac{K_r}{d}\right)e^{-\varepsilon c_8}\Phi * \quad (21)$$

$$u^*\left(\frac{\partial \chi^*}{\partial x^*}\right)e^{\varepsilon(c_1 - c_4 - c_9)} + v^*\frac{\partial \chi^*}{\partial y^*}e^{\varepsilon(c_2 - c_5 - c_9)} + w^*\frac{\partial \chi^*}{\partial z^*}e^{\varepsilon(c_3 - c_6 - c_9)} + \left(\frac{bW_c}{\nu}\right)\left[\left(\frac{N_\infty}{N_w - N_\infty}\right)\left(\frac{\partial^2 \chi}{\partial {z^*}^2}\right)e^{\varepsilon(2c_3 - c_9)}\right] + \left(\frac{bW_c}{\nu}\right)\left[\left(\frac{\partial^2 \Phi}{\partial {z^*}^2}\right)e^{\varepsilon(2c_3 - c_8 - c_9)} + \left(\frac{\partial \chi^*}{\partial z^*}\right)\left(\frac{\partial \Phi^*}{\partial z^*}\right)e^{\varepsilon(2c_3 - c_8 - c_9)}\right] = \left(\frac{D_N}{\nu}\right)\left(\frac{\partial^2 \chi}{\partial {z^*}^2}\right)e^{\varepsilon(2c_3 - c_9)} - \left(\frac{K_r}{d}\right)e^{-\varepsilon c_9}\chi^* \quad (22)$$

B.C's (10) become

$$At\ y\ =\ 0, \left(\frac{\partial \psi^*}{\partial y^*}\right) e^{\varepsilon(c_2-c_4)}\ =\ \gamma^*\ x^*\ e^{-\varepsilon(c_1+c_7)},$$
$$\left(\frac{\partial \psi^*}{\partial x^*}\right) e^{\varepsilon(c_1-c_4)} = -\left(\frac{v_w^*}{\sqrt{\nu\ b}}\right) e^{-\varepsilon(c_8)},\ e^{-\varepsilon(c_5)} g^* = 1,$$
$$D_B C_\infty \left(\frac{\partial h^*}{\partial y^*}\right) e^{\varepsilon(c_2-c_6)} + \left(\frac{D_T}{T_\infty}\right)(T_w - T_\infty)\left(\frac{\partial g^*}{\partial y^*}\right) e^{\varepsilon(c_2-c_5)} = 0, \quad (23)$$
$$and\ \left(\frac{\partial \psi^*}{\partial y^*}\right) e^{\varepsilon(c_2-c_4)} = 0,\ \left(\frac{\partial \psi^*}{\partial x^*}\right) e^{\varepsilon(c_1-c_4)} = 0,$$
$$e^{-\varepsilon(c_5)} g^* = 0,\ e^{-\varepsilon(c_6)} h^* = 0,\ as\ y \to \infty$$

The following relations has been derived from group of transformation

$$c_1\ -\ c_4\ =\ c_2\ -\ c_5\ =\ c_3\ -\ c_6 \quad (24)$$

$$c_1 - 2c_4 = c_2 - c_4 - c_5 = c_3 - c_4 - c_6 = 2c_5 - c_4 = -c_4 \quad (25)$$

$$c_3 - c_5 = c_1 + c_2 - c_4 - c_5 = 2c_2 - c_5 = 2c_2 - c_5 - c_6 = 2c_2 - 2c_5 \quad (26)$$

$$c_3 - c_6 = c_1 + c_2 - c_4 - c_6 = 2c_2 - c_6 = 2c_2 - c_5 \quad (27)$$

$$c^2\ -\ c^4\ =\ -c_1\ -\ c_7 \quad (28)$$

$$c_1\ -\ c_4\ =\ -c_8 \quad (29)$$

$$c_5\ =\ 0 \quad (30)$$

$$c_2\ -\ c_6\ =\ c_2\ -\ c_5 \quad (31)$$

Above relations give following solutions

$$c_1\ =\ c_4, c_2\ =\ 0, c_3\ =\ 0, c_5\ =\ 0, c_6\ =\ 0,\ c_7\ =\ -c_3, c_8\ =\ 0, c_9\ =\ 0 \quad (32)$$

Set of transformation reduces to

$$x = e^{-\varepsilon c_1} x^*,\ y = e^{-\varepsilon c_2} y^*, z = z^*, u = e^{-\varepsilon c_1} u^*,\ v = e^{-\varepsilon c_2} v^*,\ w = w^*, \Theta = \Theta^*, \Phi = \Phi^*, \chi = \chi^* \quad (33)$$

Using the Taylor's series to expand in the power of ε and ignoring the higher power of ε results in

$$x\ =\ x^*\ /\ (1\ +\ \varepsilon c_1)\ , y\ =\ y^*\ /\ (1\ +\ \varepsilon c_2),\ z\ =\ z^*\ /\ (1\ +\ 0), u\ =\ u^*\ /\ (1\ +\ \varepsilon c_1),\ v\ =\ v^*\ /\ (1\ +\ \varepsilon c_2), w\ =\ w^*\ /\ (1\ +\ 0) \quad (34)$$

or

$$x^* = x(1+\varepsilon c_1),\ y^* = y(1+\varepsilon c_2),\ z^* = z(1+0),\ u^* = u(1+\varepsilon c_1),\ v^* = v(1+\varepsilon c_2),\ w^* = w(1+0) \quad (35)$$

The following characteristic equations are obtained by applying Taylor's approach to extend in powers of ε while maintaining terms up to the order ε.

$$dx/(c_1 x) = dy/(c_2 y) = dz/0 = du/(c_1 u) = dv/(c_2 v) = dw/0 \quad (36)$$

On solving the above equations we obtain the similarity transformation,

$$\eta = z,\ u = x\ f'(\eta),\ v = y\ g'(\eta),\ w = -[f(\eta) + g(\eta)],\ \Theta = \Theta(\eta),\ \Phi = \Phi(\eta),\ \chi = \chi(\eta) \quad (37)$$

Equations (7)-(9) take the form O.D.E's:

$$(1+1/\beta) f''' - (f')^2 + (f+cg)\ f'' - [M + k_1(1+1/\beta)]\ f' = 0 \quad (38)$$

$$(1+1/\beta) g''' - (g')^2 + (f+cg) g'' - [M + k_1(1+1/\beta)] g' = 0 \quad (39)$$

$$\Theta'' + Pr[(f\ +\ cg)\Theta' + Nb\ \Theta'\Phi' + Nt\ (\Theta')^2] = 0 \quad (40)$$

$$\Phi'' + LePr(f+cg)\Phi' + (Nt/Nb)\Theta'' - LePr\ C_r \Phi = 0 \quad (41)$$

$$\chi'' - Pe[(\sigma + \chi)\Phi'' + \chi'\Phi'] + PrLb(f+cg)\chi' - PrLb\ C_r\ \chi = 0 \quad (42)$$

Transformed B.C's are:

$$At\ \zeta\ =\ 0;\ f(0,\tau) =\ \alpha, \frac{df}{d\zeta}(0,\tau) =\ \gamma, g(0,\tau) =\ 1,\ Nb\frac{\partial h}{\partial \zeta}(0,\tau) +\ Nt\frac{\partial g}{\partial \zeta}(0,\tau) =\ 0 \quad (43)$$
$$As\ \zeta \to \infty;\ \partial f/\partial \zeta\ (\zeta,\tau) = 0,\ g(\zeta,\tau) = 0,\ h(\zeta,\tau) = 0$$

NUMERICAL SOLUTION

System of ODE's (10)-(14) along with (15) solved numerically due to highly non-linear behavior because it is not an easy task to solve these mathematical equations containing crucial fluid parameters analytically. To solve these equations numerically, RKF-shooting algorithm is adopted by converting these equations into a set of initial value problems as shown in Figure 2.

$$f''' = 1/(1+1/\beta)[\ f'^2 - (f+cg)f'' + k_1(1+1/\beta)f' + Mf'] \quad (44)$$

$$g''' = 1/(1+1/\beta)[g'^2 - (f+cg)g'' + k_1(1+1/\beta)g' + Mg'] \quad (45)$$

$$\Theta'' = -Pr[(f+cg)\Theta' + Nb\ \Theta'\Phi' + Nt(\Theta')^2] \quad (46)$$

$$\Phi'' = -LePr(f+cg)\Phi' - (Nt/Nb)\Theta'' + LePr\ C_r\ \Phi \quad (47)$$

$$\chi'' = Pe[(\sigma + \chi)\Phi'' + \chi'\Phi'] - PrLb(f+cg)\chi' + PrLb\ C_r\ \chi \quad (48)$$

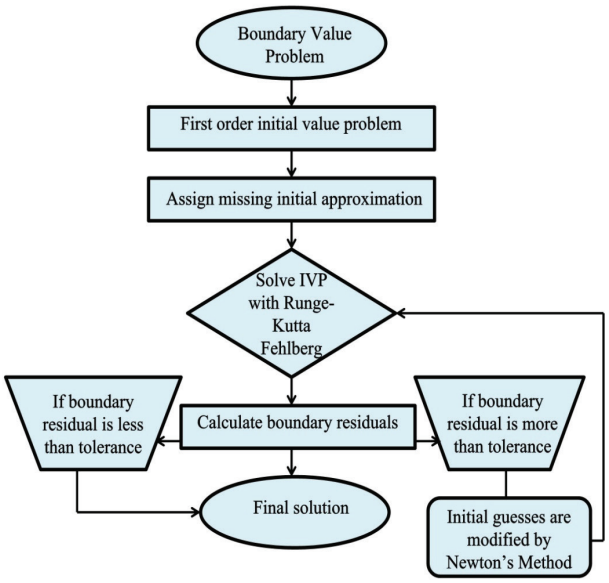

Figure 2. Flow chart of "Shooting Technique".

After being transformed into a system of first-order D.E's, the coupled differential equations are explained as follows:

$$p(1)' = p(2) \tag{49}$$

$$p(2)' = p(3) \tag{50}$$

$$p(3)' = 1/(1-\alpha {r_1}^2)[\, {r_2}^2 + M\, r_2 - (1+\beta M)\, r_1 r_3 - 2\alpha_1\, r_1\, r_2\, r_3\,] \tag{51}$$

$$p(4)' = p(5) \tag{52}$$

$$p(5)' = p(6) \tag{53}$$

$$p(6)' = 1/(1-\alpha {r_1}^2)[\, {r_2}^2 + M\, r_2 - (1+\beta M)\, r_1\, r_3 - 2\alpha_1\, r_1\, r_2\, r_3\,] \tag{54}$$

$$p(7)' = p(8) \tag{55}$$

$$p(8)' = -(3/(3+4N_r))[\, Pr\, r_1 r_5 + PrNb\, r_5 r_7 + PrNt\, {r_5}^2 + Pr\lambda\, r_4\,] \tag{56}$$

$$p(9)' = p(10) \tag{57}$$

$$p(10)' = -Le\, r_1 r_7 - (Nt/Nb)\, {r_5}' + Le\beta\, r_6 \tag{58}$$

$$p(11)' = p(12) \tag{59}$$

$$p(12)' = -Le\, r_1 r_7 - (Nt/Nb)\, r_5' + Le\beta\, r_6 \tag{60}$$

with the initial conditions $p_1 = \alpha,\ p_2 = \gamma,\ p_3 = x(1), p_4 = 1,\ p_5 = x(2)$
where

$$\begin{gathered} f = p(1), f' = p(2), f'' = p(3), f''' = p(3)' \\ g = p(4), g' = p(5), g'' = p(6), g''' = p(6)' \\ \Theta = p(7), \Theta' = p(8), \Theta'' = p(8)' \\ \Phi = p(9), \Phi' = p(10), \Phi'' = p(10)' \\ \chi = p(11), \chi' = p(12), \chi'' = p(12)' \end{gathered} \tag{61}$$

RESULTS AND DISCUSSION

In present analysis, numerical scheme is validated as calculated results for -$\Theta'(0)$ are compared with Abolbashari et al. [42], Gorla and Sidawi [43], Mankinde and Aziz [44] and Khan and Pop [45] for controlling fluid parameter *Pr* in the absence of magnetohydrodynamic flow (See Table 1). Additionally, bar graph has been plotted for these values as well to seen accuracy of the numerical technique (See Figure 3). It is observed that results obtained are highly accurate when compared with the existing literature outcomes. Moreover, Table 2-5 represents the resulting outcomes of ($f''(0), g''(0)$), -$\Theta'(0)$, -$\Phi'(0)$, and -$\chi'(0)$ respectively for fixed values of controlling fluid parameters $Pe = 0.1$, $\kappa = 0.5$, $Lb = 0.5$, $Bi_3 = 0.1$, $Bi_1 = 0.4$, $Bi_2 = 0.1$, $K_1 = 0.1$, $C_r = 0.7$, $\beta = 0.1$, $M = 1.5$, $Pr = 1.732$, $Nb = 0.1$, $Nt = 0.5$, $Le = 2.0$ along with CPU time observed in seconds.

Table 1. A comparison for -$\Theta'(0)$ against *Pr*

Pr	Abolbashari et al. [42]	Residual error	Gorla and Sidawi [43]	Residual error	Mankinde and Aziz [44]	Residual error	Khan and Pop [45]	Residual error	Present Results
0.7	0.4539	-0.00055	0.5349	-0.00055	0.4539	-0.00055	0.4539	-0.00055	0.45445
2.0	0.9114	-0.00055	0.9114	-0.00055	0.9114	-0.00055	0.9113	-0.00005	0.91135
7.0	1.8954	0.00000	1.8905	-0.00490	1.8954	0.00000	1.8954	0.00000	1.89540
20.0	-	-	3.3539	0.00000	-	-	3.3539	0.00000	3.35390
70.0	-	-	6.4622	0.00001	-	-	6.4621	-0.00009	6.46219

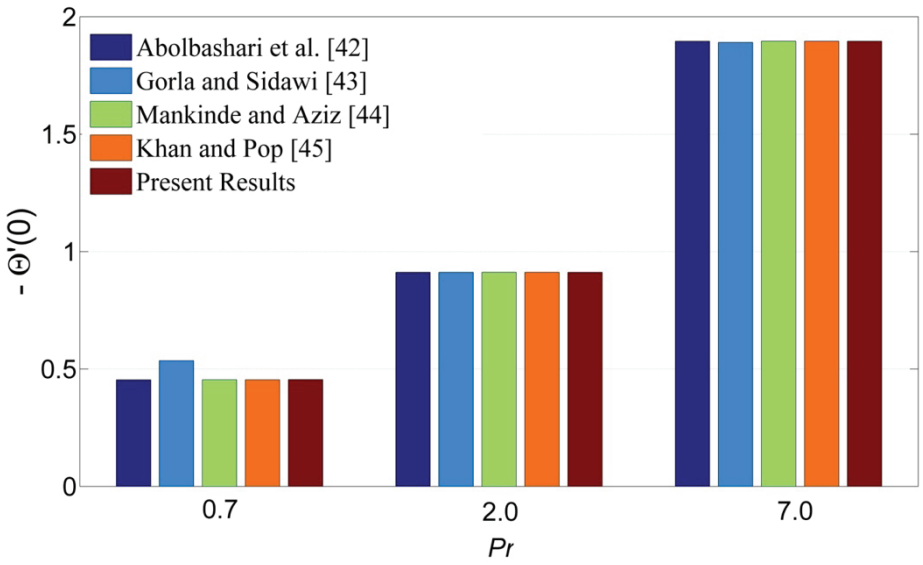

Figure 3. Bar Graph showing comparison of resulting outcomes for $-\Theta'(0)$ against three different values of Prandtl number as 0.7, 2.0 and 7.0 with those of Abolbashari et al. [42], Gorla and Sidawi [43], Mankinde and Aziz [44] and Khan and Pop [45]. [Created by authors]

Velocity Distribution

Figure 4(a)-4(f) elucidates the axial $f'(\xi)$ and transverse $g'(\xi)$ velocity distribution against crucial fluid parameters namely magnetic parameter M, Casson fluid parameter β and permeability parameter K_1 in direction of x and y-axis. Figure 4(a) and 4(b) manifests the variation in velocity distribution $f'(\xi)$ and $g'(\xi)$ against the parameter M in the range 1.5-3.5. These graphs show that with augmentation in the values of M, velocity profile falls slowly with a small variation due to produced Lorentz drag force. Additionally, it has been noticed that both the magnitude as well as width of boundary layer of $f'(\xi)$ and $g'(\xi)$ lessens with enhancement in M as shown in Figures 4(a) and 4(b) serially.

Also, Figures 4(c) and 4(d) shows the variation in velocity under the impact of Casson fluid parameter for

Table 2. Values of Cf_x and Cf_y for precised entries of M, β and K_1 with CPU time in seconds

M	β	K_1	Cf_x	Cf_y	CPU Time (In Seconds)
1.5			-0.624727	-0.671375	6.273146
2.0			-0.659909	-0.704250	9.130985
2.5			-0.693344	-0.735688	18.056714
3.0			-0.725266	-0.765856	20.579231
3.5			-0.755859	-0.794896	23.093199
	0.1		-0.624727	-0.671375	6.318504
	0.3		-0.915383	-0.995628	44.357009
	0.5		-1.079947	-1.178022	9.799734
	0.7		-1.190544	-1.300355	10.196454
	0.9		-1.271079	-1.389346	21.929840
		0.1	-0.624727	-0.671375	6.292501
		0.2	-0.699843	-0.741818	19.204972
		0.3	-0.767759	-0.806223	15.034273
		0.4	-0.830195	-0.865899	30.920958
		0.5	-0.888286	-0.921749	35.860811

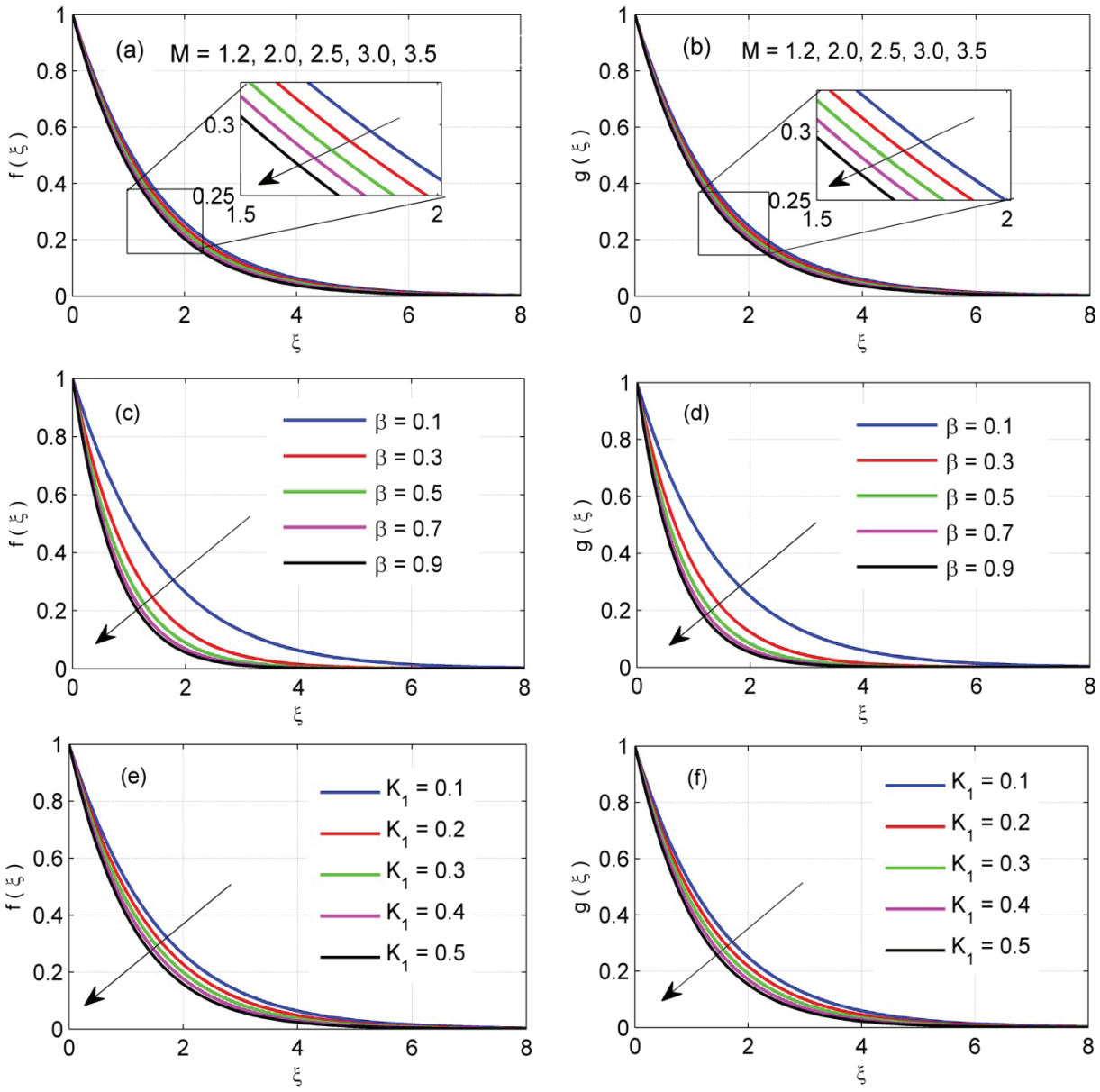

Figure 4. Axial and Transverse velocity distribution against (a, b) Magnetic parameter M ($1.2 \leq M \leq 3.5$), (c, d) Casson fluid parameter β ($0.1 \leq \beta \leq 0.9$) and (e, f) permeability parameter K_1 ($0.1 \leq K_1 \leq 0.5$.

β = 0.1, 0.3, 0.5, 0.7, 0.9. . Same behavior of velocity has been noticed i.e. declines for higher β in both the graphs like magnetic parameter and permeability parameter K_1. Reason behind declination in fluid velocity is the shear stress which is highly produced in non-Newtonian fluid when compared with Newtonian fluids. As Casson fluid is considered as non-Newtonian thus produces high stress and fluid resistance. Hence, this more non-Newtonian behavior helps in reduction of fluid velocity. Furthermore, the influence of permeability parameter K_1 ($0.1 \leq K_1 \leq 0.5$) over velocity profile has been illustrated via Figures 4(e) and 4(f) respectively. Both the velocity profiles i.e. axial and transverse declines when K_1 rises due to presence of more nanofluid far from boundary which shows the reduction in boundary layer thickness for both $f'(\xi)$ and $g'(\xi)$.

Temperature Distribution

Figure 5(a)-5(d) represent the variation in temperature against controlling fluid parameters especially Brownian motion parameter Nb in the range 0.1-5.0, thermophoresis parameter in the range 0.5-2.5, thermal Biot number in the range 0.1-2.0 and Prandtl number in the range 0.732-20. Figure 5(a) exhibits the nanoparticle

temperature profile $\Theta(\xi)$ for *Nb*. As Brownian motion is the random motion of poised particles which is produced by the collision of pendulous particles in the fluid that simultaneously helps to rise the boundary layer thickness. Consequently, higher values of *Nb* enhances nanoparticles movement that increases kinetic energy and hence temperature field rises (See Figure 5(a)) and local Nusselt number reduces (See Table 3). Moreover, larger values of *Nb* thickens the thermal boundary layer. Variation in the profile of temperature against thermophoresis *Nt* is sketched via Figure 5(b). This figure elaborates that, higher *Nt* ($0.5 \leq Nt \leq 2.5$) makes movement of nanoparticles from hot to cold zone due to temperature gradient and demonstrate stronger thermophoretic force that consequently mounting temperature profile. Further, Figure 5(c) manifests the impact of Biot number Bi_1 over nanoparticle temperature field. With increase in Bi_1, a rapid augmentation in fluid temperature is observed near the boundary. In addition, convective heating of 3D permeable sheet rises with rise in thermal Biot number. Moreover, it is observed that all plots are declines distinctly upto $\xi = 2.6$ in approx manner and convergence meets to $\xi \to \infty$. Variation in temperature distribution $\Theta(\xi)$ under influence of Prandtl number *Pr* is illustrated via Figure 5(d) and the corresponding values of local Nusselt number for *Pr* at 0.732, 7, 10, 15 and 20 are shown in Table 3. *Pr* is characterized as the ratio of two controlling parameters namely; momentum and thermal diffusivity. Nature of *Pr* is opposite to the *Nb* and *Nt* i.e. rate of thermal diffusion declines in case of higher Prandtl number due to viscous diffusion at higher level which is the main reason thinning of thermal boundary layer.

Concentration Distribution

Concentration profile for Brownian motion *Nb* varies from 0.1-5.0, thermophoresis *Nt* varies from0.5-2.5, concentration Biot number Bi_2 varies from 1.0-5.0, Prandtl number *Pr* varies from 0.732-20, Lewis number *Le* varies from 1.0-20.0 and chemical reaction parameter C_r varies from 0.0-4.0 are depicted graphically via Figures 6(a)-6(f). Figure 6(a) examines the variation in nanofluid concentration field under the impact of *Nb* for five different values of *Nb* as 0.1, 1.0, 2.0, 3.0, and 5.0. Concentration profile for Brownian motion *Nb* varies from 0.1-5.0, thermophoresis *Nt* varies from 0.5-2.5, concentration Biot number Bi_2 varies from 1.0-5.0, Prandtl number *Pr* varies from0.732-20, Lewis number *Le* varies from 1.0-20.0 and chemical reaction parameter C_r (varies from 0-4.0 are depicted graphically via Figures 6(a)-6(f). Figure 6(a) examines the variation in nanofluid concentration field under the impact of *Nb* for five different values of *Nb* as 0.1, 1.0, 2.0, 3.0, and 5.0. Augmentation in *Nb* will reduces the nanoparticle concentration and in consequence

Table 3. Values of Nu_x for precised entries of *Nb*, *Nt*, Bi_1, and *Pr* with CPT time (in seconds)

Nb	*Nt*	Bi_1	*Pr*	Nu_x	CPU Time (In Seconds)
0.1				-0.283901	6.089723
1				-0.282024	6.054968
2				-0.279908	6.082267
3				-0.277759	7.164895
5				-0.273362	6.218876
	0.5			-0.283901	6.278092
	1			-0.279169	6.280475
	1.5			-0.274205	6.545353
	2			-0.269000	7.345515
	2.5			-0.263548	10.054311
		0.1		-0.091039	6.255517
		0.5		-0.329829	6.191972
		1		-0.484207	6.356057
		1.5		-0.570896	7.425508
		2		-0.625831	9.700599
			0.732	-0.284022	6.151001
			7	-0.350411	7.310118
			10	-0.355914	7.699206
			15	-0.360854	8.515512
			20	-0.363515	9.228643

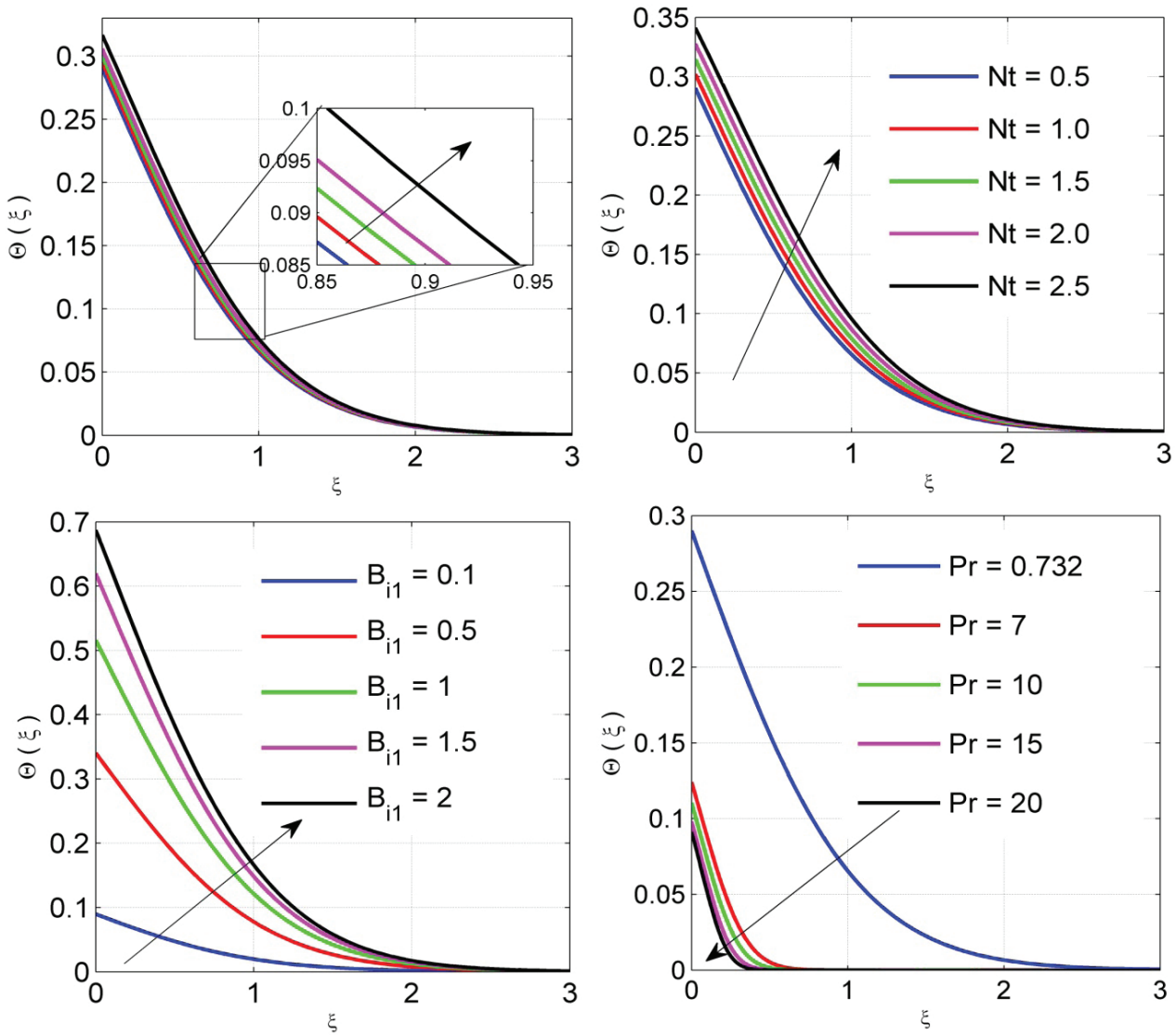

Figure 5. Temperature distribution against (a) Nb ($0.1 \leq Nb \leq 5.0$), (b) Nt ($0.5 \leq Nt \leq 2.5$), (c) Bi_1 ($0.1 \leq Bi_2 \leq 2.0$) and Pr ($0.732 \leq Pr \leq 20.0$).

solutal boundary layer thickness falls down. Additionally, slightly increase in Sherwood number is observed with enhancement in Nb as seen in Table 4. Also, the influence of Nt over nanoparticle concentration distribution is illustrated through Figure 6(b). This figure elaborates that higher Nt rises the mass distribution or concentration of the fluid. Physically, temperature gradient gives mass field and this Nt parameter makes temperature to be a mounting function of Nt. Thusly, an enhancement in mass and mass boundary layer thickness has been noticed with enhancement in Nt. Figure 6(c) illustrates the impact of concentration Biot number Bi_2 ($1.0 \leq Bi_2 \leq 5.0$) over nanoparticle concentration field. This figure shows that, concentration of nanofluid rises with rise in Bi_2. Because higher Biot number will enhances convective heating at the surface of three dimensional stretching sheet. As mass field is influences via energy field, one explained that a deeper mass dispersion is observed for higher Bi_2 values and can be seen in Figure 6(c). Additionally, all plots of the figure falls distinctly upto $\xi = 3$ (approximately) and follows convergence criterion. Effect of Pr over nanoparticle concentration has been illustrated via Figure 6(d). As Pr is inversely proportional to thermal diffusivity which indirectly leads to enhance value of Prandtl number with lower diffusivity value and in consequence plays a major role in declination of temperature and concentration of the nanofluid. Hence, higher Pr declines concentration and simultaneously helps to increase local Sherwood number

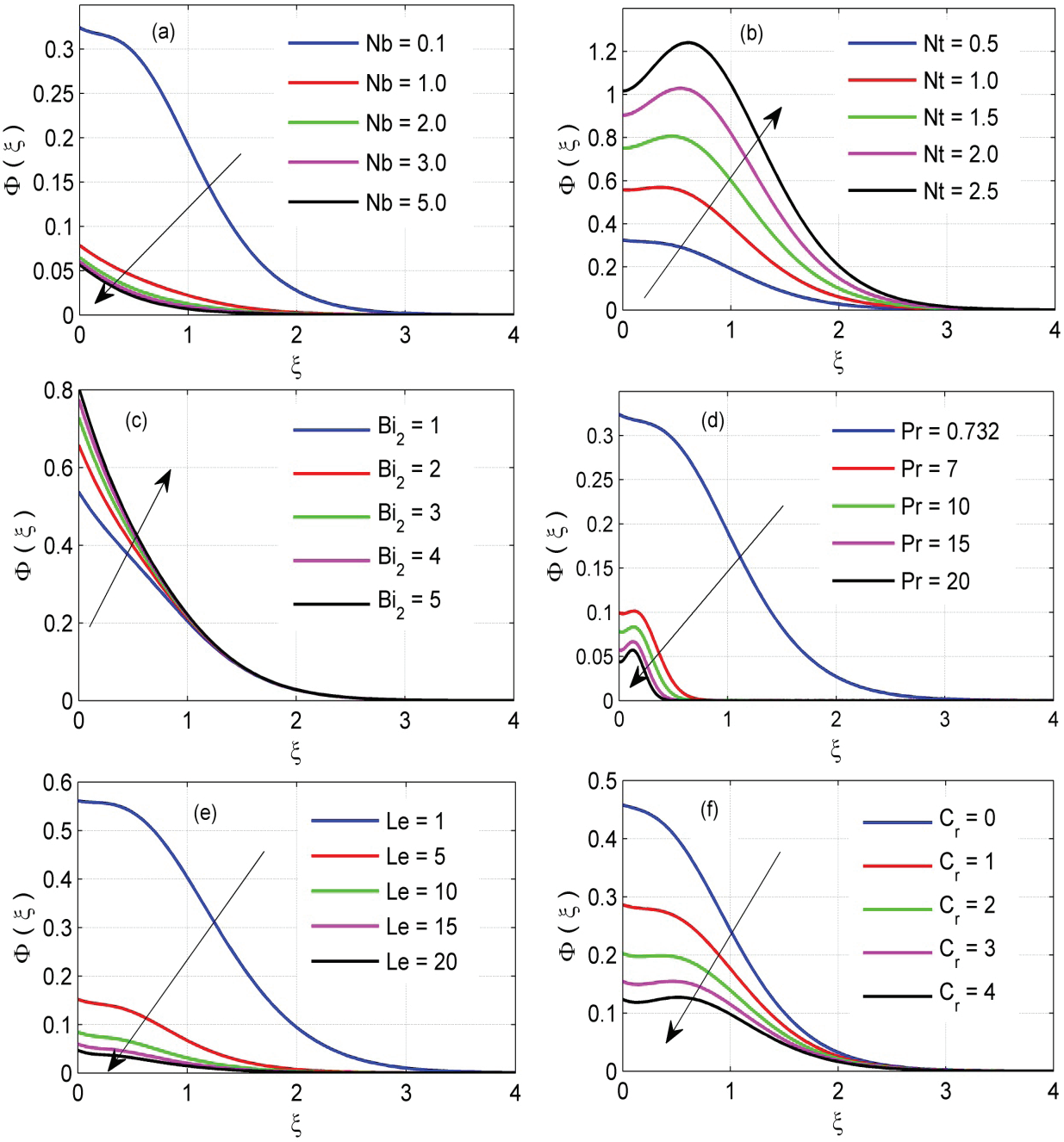

Figure 6. Concentration distribution against (a) *Nb* ($1.0 \le Nb \le 5.0$), (b) *Nt* ($0.5 \le Nt \le 2.5$), (c) Bi_2 ($1.0 \le Bi_2 \le 5.0$) and *Pr* ($0.732 \le Pr \le 20.0$), (e) *Le* ($1.0 \le Le \le 20$ and (*f*) C_r ($0.0 \le C_r \le 4.0$).

as shown in Table 4. Lewis number is the ratio of α (thermal diffusivity) and D_B (Brownian diffusion coefficient) i.e. inversely proportional to D_B which in consequence shows that higher *Le* corresponds to lower D_B. Hence, nanoparticle concentration reduces for greater *Le* ($1.0 \le Le \le 20.0$) as seen in Figure 6(e) and respective Sherwood number rises as seen in Table 4. Nanoparticle concentration is mainly influenced by chemical reaction. In present analysis, chemical reaction of first order is discussed and is displayed via Figure 6(f). This figure elaborates that nanoparticle concentration decays with advancement in C_r and follows boundary conditions away from the surface, which in turns, becomes stable.

Density of motile micro-organism distribution against controlling fluid parameters especially Peclet number *Pe* in the range 0.1-10.0, micro-organism concentration

difference parameter in the range0.1-5.0, bio-convective Lewis number in the range 0.1-0.9, chemical reaction in the range 0-4.0, micro-organism Biot number in the range 1-10 and Prandtl number in the range 0.732-20 is visualized in Figure 7(a)-7(f) serially. Figure 7(a) elucidates the impact of Peclet number *Pe* on motile density $\chi(\xi)$. This plot shows that, with increase in values of *Pe* ($0.1 \leq Pe \leq 10.0$), fluid particles moves freely leads to thickens micro-organism and hence reduces the motile density of micro-organisms. Moreover, graphs are distinct within $0.0 \leq \xi \leq 5.0$ in approx manner and after that they meet and converges as $\xi \to \infty$ by following boundary conditions. variation in gyrotactic micro-organism density $\chi(\xi)$ against micro-organism concentration difference parameter κ is sketched via Figure 7(b). It is observed from the figure that $\chi(\xi)$ declines for higher values of κ because of lower micro-organism concentration difference between N_w & N_∞ and their respective local wall motile micro-organism number has same nature as that of $\chi(\xi)$ i.e. declines with augmentation in κ as seen in Table 5.

Figure 7(c) manifests the motile density against bio-convective Lewis number *Lb*. As bio-convective Lewis number is inversely proportional to the micro-organisms diffusivity D_N, which in turn enhances *Lb* value with lower D_N and hence reduces the micro-organism density of nanofluid flow as seen in Figure 7(c). However, local wall motile micro-organism number Mn_x mounting as visualized in Table 5. Also, the impact of chemical reaction parameter C_r ($0 \leq C_r \leq 4$) over motile micro-organism distribution is illustrated via Figure

Table 4. Values of Sh_x for precised entries of *b*, *Nt*, Bi_2, *Pr*, *Le* and C_r with CPU time (in seconds)

Nb	*Nt*	Bi_2	*Pr*	*Le*	C_r	Sh_x	CPU Time (In Seconds)
0.1						-0.067573	6.089723
1						-0.092147	6.054968
2						-0.093512	6.082267
3						-0.093968	7.164895
5						-0.094333	6.218876
	0.5					-0.067573	6.278092
	1					-0.044243	6.280475
	1.5					-0.024887	6.545353
	2					-0.009578	7.345515
	2.5					0.001638	10.054311
		1				-0.462481	6.229663
		2				-0.684838	7.301691
		3				-0.815543	7.113896
		4				-0.901580	7.242372
		5				-0.962506	7.291741
			0.732			-0.067611	6.151001
			7			-0.090030	7.310118
			10			-0.092146	7.699206
			15			-0.094238	8.515512
			20			-0.095561	9.228643
				1		-0.043871	6.373926
				5		-0.084811	6.177161
				10		-0.091558	6.470720
				15		-0.094015	9.267156
				20		-0.095304	14.788844
					0	-0.054220	6.968463
					1	-0.071371	7.538299
					2	-0.079754	11.180259
					3	-0.084577	15.477882
					4	-0.087651	24.767878

Motile Density Micro-Organism Distribution							
Pe	***κ***	***Lb***	C_r	Bi_3	***Pr***	Nh_x	**CPU Time (In Seconds)**
0.1						-0.089503	13.406621
1						-0.089410	15.257320
5						-0.091353	15.404992
7						-0.093223	17.983860
10						-0.096468	18.528993
	0.1					-0.089553	12.491580
	1					-0.089441	14.797041
	2					-0.089317	12.557861
	3					-0.089193	12.693556
	5					-0.088946	12.598996
		0.1				-0.077483	13.025669
		0.3				-0.086515	13.092459
		0.5				-0.089503	13.029538
		0.7				-0.091115	13.088236
		0.9				-0.092160	12.683444
			0			-0.087098	6.968463
			1			-0.090203	7.538299
			2			-0.091818	11.180259
			3			-0.092832	15.477882
			4			-0.093541	24.767878
				1		-0.461563	5.972003
				2		-0.600167	7.342002
				5		-0.732066	7.312585
				7		-0.764051	8.398161
				10		-0.789935	8.662353
					0.732	-0.089518	6.151001
					7	-0.096669	7.310118
					10	-0.097234	7.699206
					15	-0.097766	8.515512
					20	-0.098086	9.228643

7(d). Gyrotactic micro-organism distribution $\chi(\xi)$ is also influenced by chemical reaction C_r as that of nanoparticle concentration profile. Thus a decay in motile concentration is observed with enhancement in C_r. Further, Figure 7(e) represents the variation of $\chi(\xi)$ under the influence of micro-organism Biot number Bi_3 and it shows that motile density rises with rise in Bi_3 from 1.0-10.0. Consequently, intensification in local wall motile micro-organism number is noticed for higher Bi_3 (See Table 5). Figure 7(f) portraits the variation in motile density of micro-organism $\chi(\xi)$ against Prandtl number. This figure elucidates that $\chi(\xi)$ drops down suddenly when Prandtl varies from 0.732-7 and then decreases slowly from $7 \leq Pr \leq 20$. Overall reduction in $\chi(\xi)$ is observed for higher Prandtl value as seen in Figure 7(f) and their respective Mn_x increases as shown in Table 5. Additionally, graph meets its convergence criterion at $\xi = 3$ (approximately) as clearly visualized in the figure.

Local Skin Friction, Nusselt Number, Sherwood Number & Wall Motile Micro-Organism

Figure 8(a) and 8(b) examines the impact of $f''(0)$ and $g''(0)$ against controlling parameters β $(0.1 \leq \beta \leq 0.5)$ and M $(1.5 \leq M \leq 3.5)$. It is observed from the figures that, higher β declines skin friction at the wall monotonically and in addition more magnetism helps to decrease the value of skin friction as well. This is due to the reason that larger magnetism and non-Newtonian fluid reduces the velocity profile which ultimately helps to reduce skin friction coefficient as depicted in both the graphs.

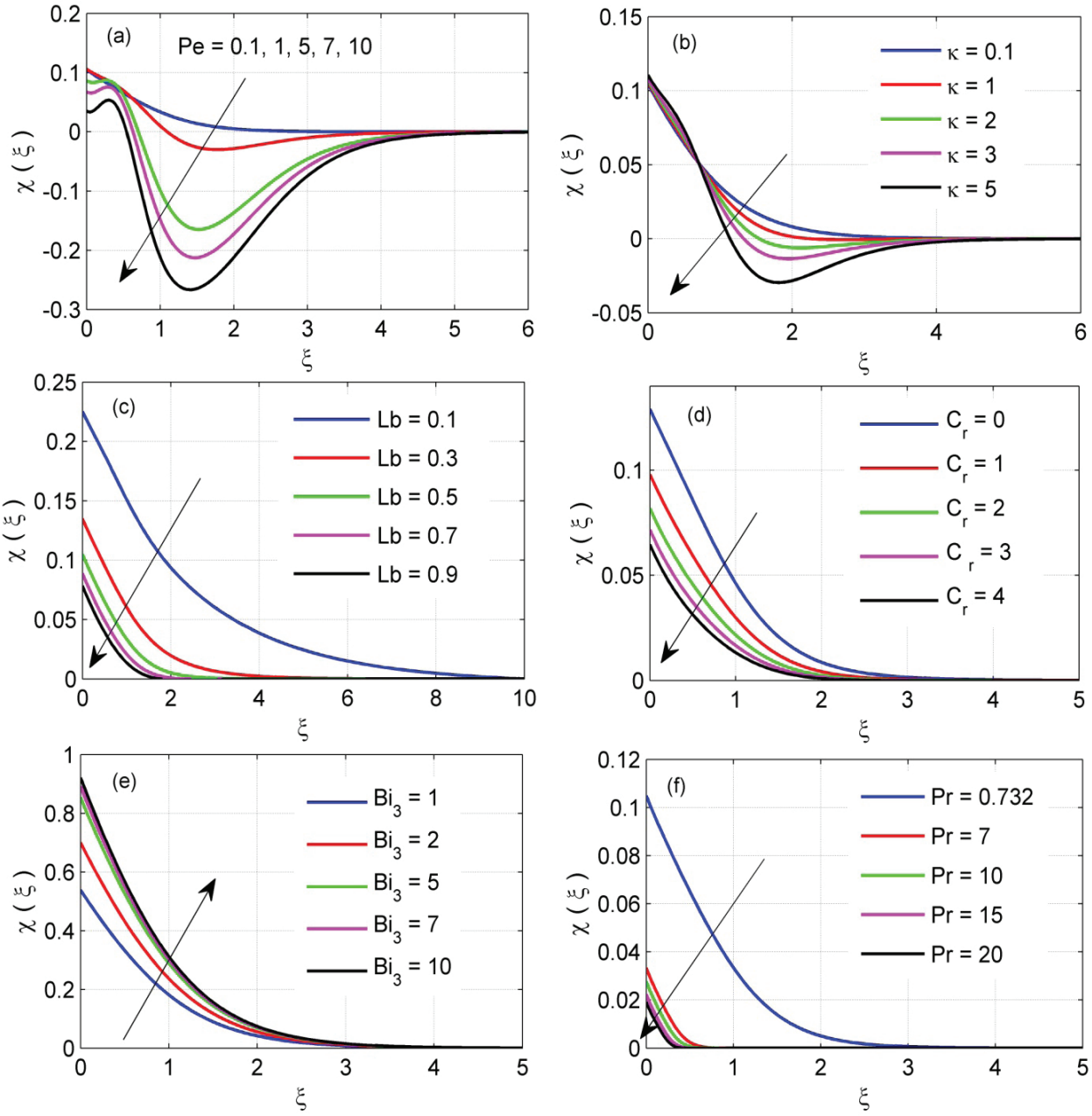

Figure 7. Motile density micro-organism distribution against (a) Pe ($0.1 \le Pe \le 10.0$), (b) κ ($1.0 \le \kappa \le 5.0$), (c) Lb ($0.1 \le Lb \le 0.9$), (d) C_r ($0 \le C_r \le 4$), (e) Bi_3 ($1 \le Bi_3 \le 10$) and (f) Pr ($0.732 \le Pr \le 20.0$).

The combined influence of Brownian motion Nb ($1 \le Nb \le 5.0$) and thermal Biot number Bi_1 ($0.5 \le Bi_1 \le 0.6$ over $-\Theta'(0)$ is elucidates via Figure 8(c). Nb and Bi_1 shows reverse impact on $-\Theta'(0)$ i.e. higher enhances $-\Theta'(0)$ due to convective heating whereas higher Nb reduces $-\Theta'(0)$ due to fast collision of nanoparticles. Also, the impact of Prandtl number Pr ($1 \le Pr \le 5$) and concentration Biot number Bi_2 ($1 \le Bi_2 \le 5$) on $-\Phi'(0)$ is sketched via Figure 8(d). Both the controlling fluid parameters Pr and Bi_2 enhances value of $-\Phi'(0)$ as clearly visualized in Figure 8(d). Combined impact of Peclet number Pe ($1 \le Pe \le 5.0$) and κ ($0.1 \le \kappa \le 0.5$) over $-\chi'(0)$ is shown by Figure 8(e) and it is observed that $-\chi'(0)$ decreases with increase in κ while rises with rise in Pe. Figure 8(f) manifests the variation in $-\chi'(0)$ against bio-convection Lewis number Lb ($0.1 \le Lb \le 0.9$) and chemical reaction C_r ($0 \le C_r \le 1$). Both the parameters enhance wall motile micro-organism number with their higher values.

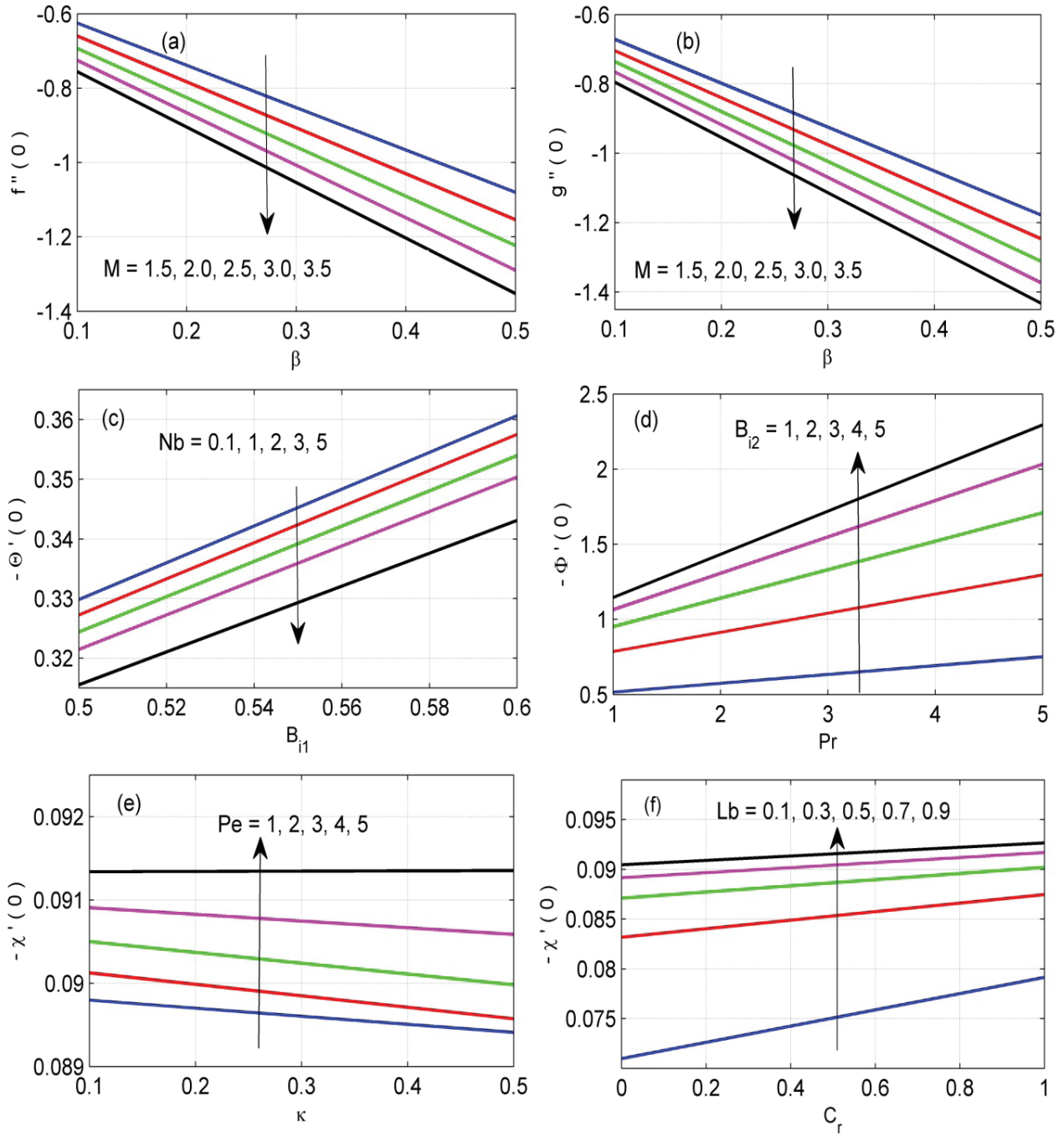

Figure 8. Graph for (a) $f''(0)$ against M & β, (b) $g''(0)$ against M & β, (c) $-\Theta'(0)$ against Nb & Bi_1, (d) $-\Phi'(0)$ against Bi_2 & Pr, (e) $-\chi'(0)$ against Pe & κ and (f) $-\chi'(0)$ against Lb & C_r.

CONCLUSION

This investigation deals with 3D flow consisting of nanoparticles along with gyrotactic microorganisms and bioconvective chemical reaction. Final outcomes of current research are summarized as:

- Horizontal velocity $f'(\xi)$ as well as transversal velocity $g'(\xi)$ declines with inclination in the values of M, β and K_1.
- Augmentation in temperature profile is noticed for greater thermal Biot number Bi_1 whereas higher Prandtl number Pr helps to falls temperature $\Phi(\xi)$.
- Concentration profile $\Phi(\xi)$ declines with higher C_r, Le, Pr, Nb. On the other hand, higher Bi_2 and Nt amplifies concentration field.

- Higher values of crucial fluid parameter Pe and κ de-escalates the motile concentration of micro-organisms.
- Skin friction coefficients $f''(0)$ & $g''(0)$ drop-off under the combined influence of controlling fluid parameters magnetic parameter M and Casson parameter β. Local wall motile micro-organism number accelerates with Lb and lessens with κ.
- Motile density Biot number falls down by 41.57% with augmentation in value of gyrotactic microorganism Biot number ranging from 1.0-10.0.

Current research can be extended for various non-Newtonian fluids by utilizing porous medium, Stefan blowing impact, entropy generation, viscous dissipation, etc.

NOMENCLATURE

x, y Cartesian coordinates
C_w Nanoparticle volume fraction (Kgm^{-3})
C Concentration (Kgm^{-3})
L Characteristic length
Le Lewis number
c Stretching parameter
β Casson fluid parameter
B_0 Magnetic field intensity (T)
Bi_3 Motile microorganism Biot number
Nu_x Nusselt number
q_m Mass flux
Nt Thermophoresis parameter
M Magnetic field parameter (Tesla)
u Horizontal velocity
C_∞ Ambient nanoparticle volume fraction (Kgm^{-3})
q_w Heat flux ($W^{-2}m$)
T_w Temperature at the sheet (K)
Bi_2 Concentration Biot number
D_T Thermophoresis diffusion coefficient (m^2s^{-1})
u_w Stretching velocity
T Temperature (K)
Nb Brownian motion parameter (m^2s^{-1})
D_B Brownian diffusion coefficient
v Vertical velocity (ms^{-1})
Sh_x Sherwood number
Pr Prandtl number
T_∞ Ambient temperature (K)
Lb Bioconvective Lewis number
Bi_1 Thermal Biot number
K_1 Permeability parameter
Mn_x Local wall motile microorganism number
Pe Peclet number

Greek symbols
ν kinematic viscosity (m^2s^{-1})
β Casson fluid parameter
σ Velocity slip parameter
ξ Similarity variable
χ Non-dimensional motile concentration
ρ_f Density of base fluid (Kgm^{-3})
Φ Non-dimensional concentration
Θ Non-dimensional temperature
τ Ratio of heat capacities
α Thermal diffusivity

Subscripts
∞ Ambient condition
p Particle
f Fluid
w Wall
Superscript
$'$ Prime denotes derivative w.r.t to ξ

AUTHORSHIP CONTRIBUTIONS

Authors equally contributed to this work.

DATA AVAILABILITY STATEMENT

The authors confirm that the data that supports the findings of this study are available within the article. Raw data that support the finding of this study are available from the corresponding author, upon reasonable request.

CONFLICT OF INTEREST

The author declared no potential conflicts of interest with respect to the research, authorship, and/or publication of this article.

ETHICS

There are no ethical issues with the publication of this manuscript.

STATEMENT ON THE USE OF ARTIFICIAL INTELLIGENCE

Artificial intelligence was not used in the preparation of the article.

REFERENCES

[1] Usman M, Amin S, Saeed A. Magnetohydrodynamic hybrid nanofluid flow with the effect of Darcy–Forchheimer theory and slip conditions over an exponential stretchable sheet. Adv Mech Eng 2022;14. [CrossRef]

[2] Asghar A, Ying TY, Zaimi K. Two-dimensional magnetized mixed convection hybrid nanofluid over a vertical exponentially shrinking sheet by thermal radiation, joule heating, velocity and thermal slip conditions. J Adv Res Fluid Mech Therm Sci 2022;95:159–179. [CrossRef]

[3] Haque MM, Alam MS, Huda MN, Rahman MM. Statistical and Numerical Investigations of Convective Heat Transfer Enhancement of Nanofluids Inside a Rectotrapezoidal Enclosure in

the Presence of Horizontal Periodic Magnetic Field. Arab J Sci Eng 2024;1–24. [CrossRef]

[4] Bilal M, Waqas M, Shafi J, Rahman MU, Eldin SM, Alaoui MK. Energy transmission through radiative ternary nanofluid flow with exponential heat source/sink across an inclined permeable cylinder/plate: numerical computing. Sci Rep 2023;13:22204. [CrossRef]

[5] Algehyne EA, Areshi M, Saeed A, Bilal M, Kumam W, Kumam P. Numerical simulation of bioconvective Darcy Forchhemier nanofluid flow with energy transition over a permeable vertical plate. Sci Rep 2022;12:3228. [CrossRef]

[6] Takreem KM, Narayana PVS. Nanoparticle Shape-Factor Analysis on Radiative Ternary Nanofluid (Mwcnt- Cu- Sio 2/H 2 O) Flow with Non-Fourier Thermal Flux. J Porous Media 2025;28. [CrossRef]

[7] Rafique E, Iram A, Jahan S, Sohail M, Sherif ESM. Bio-convective flow of non-Newtonian Williamson nanofluid model with heat generation and thermal radiation aspects past over a stretched porous sheet via OHAM. Multiscale Multidiscip Model Exp Des 2025;8:45. [CrossRef]

[8] Afzal F, Kamran T. Advanced heat transfer analysis of 3D magnetohydrodynamic nanofluid flow over an extending sheet with thermal radiation and internal heat generation/absorption. Multiscale Multidiscip Model Exp Des 2025;8:113. [CrossRef]

[9] Atofarati EO, Sharifpur M, Huan Z. Nanofluids for heat transfer enhancement: a holistic analysis of research advances, technological progress and regulations for health and safety. Cogent Eng 2024;11:2434623. [CrossRef]

[10] Jubair S, Ali B, Rafique K, Mahmood Z, Emam W. Numerical simulation of hybrid nanofluid flow with homogeneous and heterogeneous chemical reaction across an inclined permeable cylinder/plate. Energy Explor Exploit 2024;42:2270–2288. [CrossRef]

[11] Casson N. Flow equation for pigment-oil suspensions of the printing ink-type. Rheology of disperse systems 1959;84–104.

[12] Rao PS, Prakash O, Mishra SR, Sharma RP. Similarity solution of three-dimensional MHD radiative Casson nanofluid motion over a stretching surface with chemical and diffusion-thermo effects. Heat Transf 2020;49:1842–1862. [CrossRef]

[13] Ramamoorthy M, Pallavarapu L. Radiation and Hall effects on a 3D flow of MHD Williamson fluid over a stretchable surface. Heat Transf 2020;49:4410–4426. [CrossRef]

[14] Makkar V, Poply V, Goyal R, Sharma N. Numerical investigation of mhd casson nanofluid flow towards a non linear stretching sheet in presence of double-diffusive effects along with viscous and ohmic dissipation. J Therm Eng 2021;7:1–17. [CrossRef]

[15] Megahed AM. Williamson fluid flow due to a non-linearly stretching sheet with viscous dissipation and thermal radiation. J Egypt Math Soc 2019;27:12. [CrossRef]

[16] Zeeshan A, Khan MI, Ellahi R, Marin M. Computational intelligence approach for optimising MHD Casson ternary hybrid nanofluid over the shrinking sheet with the effects of radiation. Appl Sci 2023;13:9510. [CrossRef]

[17] Waseem M, Jawad M, Aldalbahi MM, Naeem S, Gull H, Majeed A. Statistical and mathematical modeling of viscoelastic 3D Casson nanofluid flow with activation energy and motile microbes induced by exponential sheet bounding with Darcy-Forchheimer porous medium. Multiscale Multidiscip Model Exp Des 2025;8:14. [CrossRef]

[18] Swain S, Swain BK, Sahoo B. Application of homotopy perturbation method on special third grade fluid flow with viscous dissipation effect over a stretching sheet. Int J Mod Phys C 2023;34:2350060. [CrossRef]

[19] Swain BK, Kar S. Dissipative MHD flow of ternary-hybrid nanofluid over an inclined stretching sheet with heat source and mass flux due to temperature gradient. ZAMM Z fur Angew Math Mech 2024;104:e202200360. [CrossRef]

[20] Sahoo CS, Swain BK, Das M, Dash GC. Entropy generation and porosity effects on MHD hybrid nanofluid mixed convective flow over an inclined plate in the presence of thermophoresis and heat flux. J Braz Soc Mech Sci Eng 2025;47:1–13. [CrossRef]

[21] Varatharaj K, Tamizharasi R, Sivaraj R, Vajravelu K. Simulation of MHD-Casson hybrid nanofluid dynamics over a permeable stretching sheet: effects of heat transfer and thermal radiation. J Therm Anal Calorim 2024;149:8693–8711. [CrossRef]

[22] Ali A, Hussain S, Ashraf M. Theoretical investigation of unsteady MHD flow of Casson hybrid nanofluid in porous medium: Applications of thermal radiations and nanoparticle. J Radiat Res Appl Sci 2024;17:101029. [CrossRef]

[23] Lone SA, Bossly R, Alduais FS, Al-Bossly A, Khan A, Saeed A. Blood Based Magnetohydrodynamic Casson Hybrid Nanofluid Flow on Convectively Heated Bi-Directional Porous Stretching Sheet with Variable Porosity and Slip Constraints. Chin Phys B 2024;34. [CrossRef]

[24] Elhag SH. Numerical Study on 3D MHD Darcy-Forchheimer Flow Caused by Gyrotactic Microorganisms of the Bio-Convective Casson Nanofluid across a Stretched Sheet. Front Heat Mass Transf 2024;22:377–395. [CrossRef]

[25] Dang K, Makkar V, Sharma N. Numerical analysis of three-dimensional magnetohydrodynamics non-Newtonian free stream flow induced by permeable stretching surface. J Therm Eng 2021;10:1465–1479. [CrossRef]

[26] Sowmiya C, Kumar BR, Bég OA, Kuharat S. Modeling and analysis of MHD free convective thermo-solutal transport in casson fluid flow with radiative heat flux. J Therm Anal Calorim 2024;1–15. [CrossRef]
[27] Irshad S, Jahan S, Machado JM, Śliwiński P, Kedzia K, Jan AZ. MHD Casson flow across a stretched surface in a porous material: a numerical study. Multiscale Multidiscip Model Exp Des 2025;8:36. [CrossRef]
[28] Mehmood Y, Abbasi W, Alhussein M, Aurangzeb K, Rehman A, Anwar MS. Computational behavior of trihybrid Casson nanofluid blood flow occurring inside the conical gap between the rotating disk and the cone. Contemp Math 2025;1–26. [CrossRef]
[29] Azar AA, Jalili P, Jalili B, Ganji DD. The comprehensive analysis of magnetohydrodynamic Casson fluid flow with rectangular porous medium through expanding/contracting channel. Multidiscip Model Mater Struct 2025;21:68–97. [CrossRef]
[30]. Lie S, Hermann R. Sophus Lie's 1884 differential invariant paper. Math Sci Press 1976.
[31] Pakdemirli M, Yurusoy M. Similarity transformations for partial differential equations. SIAM review 1998;40:96–101. [CrossRef]
[32] Zheng M, Nie W, Cheng D, Yu L. The Lie group analysis method for heat transfer in steady boundary layer flow field of nanofluid. Therm Sci 2024;29:184.
[33] Rana P, Shukla N, Bég OA, Bhardwaj A. Lie group analysis of nanofluid slip flow with Stefan Blowing effect via modified Buongiorno's Model: entropy generation analysis. Differ Equ Dyn Syst 2021;29:193–210. [CrossRef]
[34] Ch R, Pranitha J. Eminence of ferrite particle shapes in stratified nanofluids concerning the melting phenomenon: Lie group and spectral analysis. Chem Eng J Adv 2023;16:100540. [CrossRef]
[35] Thenmozhi D, Rao ME, Nagalakshmi C, Devi RR, Selvi PD. Lie similarity analysis of MHD Casson fluid flow with heat source and variable viscosity over a porous stretching sheet. Int J Thermofluids 2024;23:100804. [CrossRef]
[36] Disu AB, Salawu SO. Thermal distribution of magneto-tangent hyperbolic flowing fluid over a porous moving sheet: A Lie group analysis. J Niger Soc Phys Sci 2023;1103–1103. [CrossRef]
[37] Nabwey HA, Khan WA, Rashad AM. Lie group analysis of unsteady flow of kerosene/cobalt ferrofluid past a radiated stretching surface with Navier slip and convective heating. Math 2020;8:826. [CrossRef]
[38] Swain S, Sarkar GM, Sahoo B. Lie group and stability analysis of tangent hyperbolic fluid flow driven by a shrinking sheet. Numer Heat Transf A :Appl 2024;1–25. [CrossRef]
[39] Akbar NS, Al-Zubaidi A, Saleem S, Alsallami SA. Variable fluid properties analysis for thermally laminated 3-dimensional magnetohydrodynamic non-Newtonian nanofluid over a stretching sheet. Sci Rep 2023;13:3231. [CrossRef]
[40] Tufail MN, Saleem M, Chaudhry QA. An analysis of Maxwell fluid through a shrinking sheet with thermal slip effect: a Lie group approach. Indian J Phys 2021;95:725–731. [CrossRef]
[41] Ali S. Lie group analysis of bingham plastic flow over a straining surface in the presence of magnetohydrodynamic effects and slip conditions. Phys Scr 2024;99:065262. [CrossRef]
[42] Abolbashari MH, Freidoonimehr N, Nazari F, Rashidi MM. Analytical modeling of entropy generation for casson nano-fluid flow induced by a stretching surface. Adv Powder Technol 2015;26:542–552. [CrossRef]
[43] Gorla RSR, Sidawi I. Free convection on a vertical stretching surface with suction and blowing. Appl Sci Res 1994;52:247–257. [CrossRef]
[44] Makinde OD, Aziz A. Boundary layer flow of a nanofluid past a stretching sheet with a convective boundary condition. Int J Therm Sci 2011;50:1326–1332. [CrossRef]
[45] Khan W, Pop I. Boundary-layer flow of a nanofluid past a stretching sheet. Int J Heat Mass Transf 2010;53:2477–2483. [CrossRef]